The Journal of Chemical Physics

Aqueous films on pore surfaces mediate adsorption and transport of gases through crowded nanopores

Cite as: J. Chem. Phys. **154**, 094706 (2021); https://doi.org/10.1063/5.0039973
Submitted: 10 December 2020 • Accepted: 07 February 2021 • Published Online: 02 March 2021

Anh Phan and Alberto Striolo

The Journal of Chemical Physics ARTICLE scitation.org/journal/jcp

Aqueous films on pore surfaces mediate adsorption and transport of gases through crowded nanopores

Cite as: J. Chem. Phys. 154, 094706 (2021); doi: 10.1063/5.0039973
Submitted: 10 December 2020 • Accepted: 7 February 2021 •
Published Online: 2 March 2021

Anh Phan and Alberto Striolo[a)]

AFFILIATIONS

Department of Chemical Engineering, University College London, London WC1E 7JE, United Kingdom

Note: This paper is part of the JCP Special Topic on Fluids in Nanopores.
[a)]**Author to whom correspondence should be addressed:** a.striolo@ucl.ac.uk

ABSTRACT

Interactions of trapped reservoir gases within organic-rich and brine-bearing sedimentary rocks have direct relevance to many geoenergy applications. Extracting generalizable information from experimental campaigns is hindered by the fact that geological systems are extremely complex. However, modern computational tools offer the opportunity of studying systems with controlled complexity, in an effort to better understand the mechanisms at play. Employing molecular dynamics, we examine here adsorption and transport of gases containing CH_4 and either CO_2 or H_2S within amorphous silica nanopores filled with benzene. We explicitly quantify the effect of small amounts of water/brines at geological temperature and pressure conditions. Because of wetting, the presence of brines lessens the adsorption capacity of the aromatic-filled pore. The simulation results show salt-specific effects on the transport properties of the gases when either KCl or $CaCl_2$ brines are considered, although adsorption was not affected. The acid gases considered either facilitate or hinder CH_4 transport depending on whether they are more or less preferentially adsorbed within the pore as compared to benzene, and this effect is mediated by the presence of water/brines. Our simulation results could be used to extract thermodynamic quantities that in the future will help to optimize transport of various gases through organic-rich and brine-bearing sedimentary rocks, which is likely to have a positive impact on both hydrocarbon production and carbon sequestration applications. As a first step, a phenomenological model is presented here, which allows one to predict permeability based on interatomic energies.

INTRODUCTION

Prediction of fluid flow through fine-grained sedimentary rocks is a major concern in geosciences with transformational implications in subsurface hydrology.[1] Fine-grained sedimentary rocks are widely used as caprocks in carbon sequestration sites[2,3] and in petroleum geology, e.g., shale gas exploration and production.[4] Often, as-produced shale gas from diverse formations contain hydrogen sulfide (H_2S) at various concentrations ranging from tens to several hundred parts per million (ppm).[5–9] When H_2S is present, industrial facilities may be required for sweetening the produced gas[6,8] to avoid any harmful effects.[10] In some circumstances, it is appealing to inject both carbon dioxide (CO_2) and H_2S into the geological reservoirs,[11,12] as pioneered in the CarbFix operation in Iceland.[13] Because brine salinity and its composition strongly impact fluid migration in fine-grained sedimentary rocks, understanding and eventually quantifying these effects are crucial for effective enhanced oil recovery (EOR) strategies.[14] Recently, Kirkpatrick and his co-workers[15,16] quantified the influence of cations on the behavior of CO_2 and CO_2 mixed with methane (CH_4) confined in clay nanopores, both experimentally and computationally, and suggested that the preferential adsorption of CO_2 over CH_4 in clay nanopores is likely to displace CH_4, hence improving oil production in shale reservoirs. Greathouse *et al.*[17] also investigated the role of aqueous cations on the adsorption and dynamical properties of organic-cation complexes on clay mineral surfaces, achieving results that support the current assumptions for low salinity water flooding.

These recent contributions help identify those key factors that govern fluid transport through fine-grained sedimentary rocks, which, however, remains an unsolved puzzle,[18] notwithstanding its long-established significance in petroleum geology,[19] groundwater hydrology,[20] radioactive waste management,[21] and basin modeling.[22] The problem lies in the requirement of understanding the phenomena that regulate multi-component fluid transport in complex heterogeneous pore networks on several length scales. Nanoscale phenomena tend to be chemo-mechanical in nature due to the strong impact of aqueous chemistry on fluid–rock interactions that control fluid flow.[1] Furthermore, the presence of brines changes the behavior of confined organic compounds, potentially altering the rock-organic matter interfaces. A thorough assessment of such phenomena is challenging due to the intricate physical and chemical processes governing the fluid transport in geologic brine-bearing formations, especially in organic-rich shale caprocks that contain numerous poorly connected pockets of organic matters, potentially containing heavy oils. As a result, the fluid migration process within organic-rich and brine-bearing shale caprocks is extremely complex and not yet fully understood.

The objective of this study is to take advantage of the capabilities of modern molecular simulations and examine adsorption isotherms of multi-component systems containing CO_2, H_2S, and methane (CH_4), as well as their transport properties within amorphous silica nanopores saturated with benzene (C_6H_6) and either water (H_2O) or brines such as H_2O–KCl and H_2O–$CaCl_2$. K^+ and Ca^{2+} are the most prevalent s-block elements found in the natural world, especially in oil reservoirs, and the investigation of interactions between these cations and organic molecules has attracted considerable fundamental and applied interests.[14,23–25] The system simulated here is chosen as a model to resemble organic-rich and brine-bearing shale rocks. The study is conducted using atomistic equilibrium and non-equilibrium molecular dynamics (NEMD) simulations, building on the extensive studies conducted from many,[26–28] including our own group.[29,30] The results from the systematic analysis presented here contribute to advancing our quantitative understanding regarding the behavior of fluid systems of relevance to both the energy and the environmental sectors, as our results clearly demonstrate that reservoir gases–organic matters–rock–brine interactions and confinement effects determine the viability of geologic CO_2 storage, unconventional hydrocarbon productions, and EOR.

METHODS AND ALGORITHMS

Simulation setup

Organic-rich shales are source rocks that contain large amounts of oil and gas. To construct nano-pores representing those found in model organic-rich shale formations, we used a 13.4 × 13.4 × 15 $Å^3$ hydroxylated amorphous silica substrate with 4.5 OH nm^{-2} on its surface[31] as a unit cell. We replicated this unit cell to form two parallel silica substrates located at a distance sufficient to obtain a slit-shaped nano-pore of width ~20 Å. The X and Y dimensions of each silica slab were $L_{x,p}$ = 53.55 Å and $L_{y,p}$ = 53.15 Å, respectively. The model pore is finite along the X direction, exposed to the fluid reservoirs (see Fig. 1), while the pore is infinite along the Y direction due to periodic boundary conditions in all directions. The simulation box has its X, Y, and Z dimensions of 193.55 Å, 53.15 Å, and 31.71 Å, respectively. The pore generated following this method could symbolize nano-pores existing in some shale gas plays with tectosilicates (>30 wt. % of quartz) as main components.[32,33] To characterize organic-rich and brine-bearing sedimentary rocks, we saturated the pore with 280 C_6H_6 molecules and added 520 H_2O molecules near the silica pore surfaces (see Fig. 1). As benzene can both strongly adsorb onto the silica pore surface[30] and interact preferentially with water,[34] this model system is meant to illustrate oil-rich shale samples, which trap significant amounts of organic carbon.[35] To simulate KCl brines, six potassium (K^+) and six chloride (Cl^-) ions were randomly placed within the pore to yield an ionic strength of 0.64M. To generate $CaCl_2$ brines, we inserted two calcium (Ca^{2+}) and four Cl^- ions into the pore to maintain the ionic strength at 0.64M, as was the case for the KCl brine.

Force fields

We employed the CLAYFF force field to characterize SiO_2.[36] The hydrogen atoms of hydroxyl groups at SiO_2 surfaces were free to move, while other atoms in the substrates were constrained with a spring constant of 100 kcal/mol Å to maintain at their initial positions. CO_2, H_2S, and CH_4 molecules were modeled by the transferable potentials for phase equilibria (TraPPE) force field.[37–39] It was found that the TraPPE models for CO_2, H_2S, and CH_4 reproduce experimental data of vapor–liquid phase equilibria for both pure components and binary mixtures (CH_4–CO_2 and CH_4–H_2S), achieving high precision.[37,38] C_6H_6 molecules were modeled using

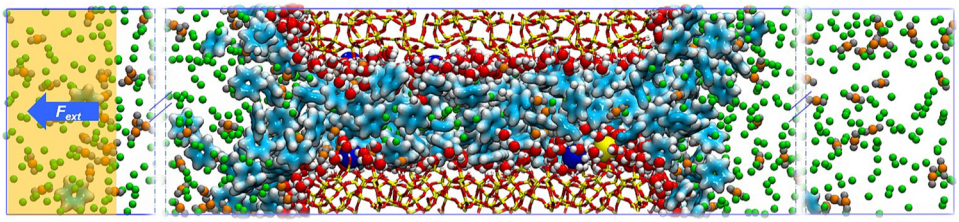

FIG. 1. Representative simulation snapshot for the amorphous silica nanopore (yellow, red, and white sticks) wetted with 520 H_2O molecules (red and white spheres), Ca^{2+}, and Cl^- (yellow and blue spheres, respectively) and filled with 280 C_6H_6 molecules (blue and white pieces), providing a model for oil-rich and brine-bearing sedimentary rocks. Green, orange, and gray spheres represent methane, carbon, and oxygen atoms of CO_2 molecules, respectively.

the second generation of the general AMBER force field (GAFF2).[40] K^+ and Cl^- ions were modeled as charged Lennard-Jones (LJ) spheres by using the parameters suggested by Dang.[41] Ca^{2+} ions were modeled as charged LJ spheres by employing the parameters reported by Predota *et al.*[42] The rigid SPC/E model was implemented to simulate H_2O[43] because of the availability of aromatic–water potentials (GAFF2-SPC/E)[44] and ion–water potentials.[41,42,45] Non-bonded atoms in systems interact via dispersive and electrostatic forces. The 12-6 LJ potentials were used to describe dispersive interactions. We employed Lorentz–Berthelot combining rules to obtain the LJ parameters for unlike interactions from the values of like components.[46] The Coulomb potential was used to model the electrostatic interactions, with the particle–particle particle–mesh (PPPM) method for treating long-range corrections.[47] We did not apply corrections for long-range LJ interactions; as such, corrections do not significantly impact the amount of fluid adsorbed in the pore studied here.

Algorithms

We performed both equilibrium and boundary-driven NEMD (BD-NEMD)[26] simulations for studying CH_4–CO_2 and CH_4–H_2S binary mixtures traveling through the pore saturated with C_6H_6 and H_2O/brine films. At first, we equilibrated the system consisting of C_6H_6 and H_2O/brine films in the presence of (a) pure CH_4 and (b) CH_4–CO_2 and CH_4–H_2S mixtures.

The equilibrium simulations lasted for 100 ns, with no external force applied. Equilibration for these simulations was confirmed by quantifying the deviations in the system properties as a function of simulation time, including energy, temperature, and CO_2, H_2S, and CH_4 density profiles along the pore. We conducted the simulations for pure CH_4 to serve as a base case against which to examine the effect of CO_2 or H_2S on CH_4 transport. Several mixtures were studied (see Table S1 of the supplementary material). We vary the numbers of CO_2 and H_2S molecules ranging from 100 to 400. The number of CH_4 molecules in each binary system was altered to keep the pressure outside the pore constant at ~13.9 MPa for all systems at equilibrium. The amount of CH_4 needed for each system was estimated by implementing the Peng–Robinson equation of state (EOS) using the molecular density of CO_2, H_2S, and CH_4 outside of the pore as inputs and customary mixing rules for multi-component mixtures.[48–50]

The BD-NEMD simulations were performed by applying an external force of 0.01 kcal/mol Å along the *X* axis to all gas molecules placed in a 20 Å slab outside of the pore (within the permeate) to impose and keep the pressure difference along the pore constant. In each simulation, we conducted 100 ns of simulations to achieve the steady state and subsequently 50 ns–70 ns of production simulations once the steady state was reached.

Implementation

Equilibrium and BD-NEMD simulations were carried out using the package LAMMPS.[51] We conducted simulations in the NVT canonical ensemble, employing the leapfrog algorithm[52] to solve the equations of motion with 1.0 fs time steps and Nosé–Hoover thermostats[53,54] to maintain the simulated temperature at 300 K with a relaxation time of 100 fs. Thermostats to fluid (CO_2, H_2S, and CH_4), solvent molecules (C_6H_6 and H_2O/brines), and the atoms in the silica substrates were applied separately.[55,56] This helped to lessen the perturbations on the system dynamics because of the application of the external force, which induces a constant energy input on fluid molecules.[29,30] We implemented the restraining potentials in PLUMED[57,58] integrated with LAMMPS during equilibrium and BD-NEMD simulations to constrain K^+/Ca^{2+} cations and Cl^- anions within the pores by introducing artificial walls placed at the pore entrances in order to keep the ionic strength fixed at 0.64M.

RESULTS AND DISCUSSION

Gas solubility and benzene displacement

To determine the relative affinity of the CH_4–CO_2 and CH_4–H_2S mixtures inside the C_6H_6-filled pore in the presence of H_2O/brine films at the pore surfaces, we estimated the solubility of CO_2, H_2S, and CH_4 within the confined systems (H_2O–C_6H_6) at 300 K using the results of equilibrium MD simulations. The left panel of Fig. 2(a) shows that CO_2 /H_2S solubility increases linearly with their bulk mole fractions (up to 0.16 and 0.24, respectively). CO_2 (empty diamonds) is less soluble in the confined H_2O–C_6H_6 system than H_2S (filled circles), yielding a solubility coefficient of 0.62 (0.04 MPa^{-1}) for CO_2 in comparison to 1.29 (0.08 MPa^{-1}) for H_2S. CO_2/H_2S solubility in the confined H_2O–C_6H_6 system is much smaller than that in confined C_6H_6 (a solubility coefficient of 0.13 MPa^{-1} and 0.33 MPa^{-1} for CO_2 and H_2S, respectively), suggesting a pronounced effect due to H_2O/brine. Compared to CO_2 and H_2S, we observe the less favorable adsorption of CH_4 within the confined system, yielding solubility coefficients from ~0.11 to 0.13 for CH_4–CO_2 and CH_4–H_2S mixtures (reported in Fig. S1 of the supplementary material). Figure 2(a), right panel, shows that loading H_2S and CO_2 into the confined system lessens CH_4 solubility. These results contrast with the fact that the presence of H_2S was found to enhance CH_4 solubility in confined C_6H_6, while CO_2 reduces such solubility (see Fig. S2 of the supplementary material), consistent with a previous study of Ref. 30. Although these observations show that the presence of H_2O/brines affects the gases solubility in the confined systems, our simulations suggest that the solubility results are not affected by the presence of either K^+/Ca^{2+} or Cl^- ions within the brines.

The number of C_6H_6 molecules confined in the nanopore decreases upon loading CO_2 (empty diamonds) and H_2S (filled circles) into the systems [see Fig. 2(b)]. Particularly, we observe that ten CO_2 molecules displace three C_6H_6 molecules, while ten H_2S molecules would replace four confined C_6H_6 molecules from the pore systems considered (see Fig. S3 of the supplementary material). Similar to previous results,[30] this indicates that the structure of organics confined in nano-pores is altered dramatically upon changing the secondary fluids in the mixture containing CH_4 and possibly accounts for significant differences in the solubility of CH_4 in confined C_6H_6 (see Fig. S2 of the supplementary material).

CO_2/H_2S transport properties

A density (/pressure) gradient is established across the pore filled with C_6H_6 and H_2O/brine films via implementing BD-NEMD

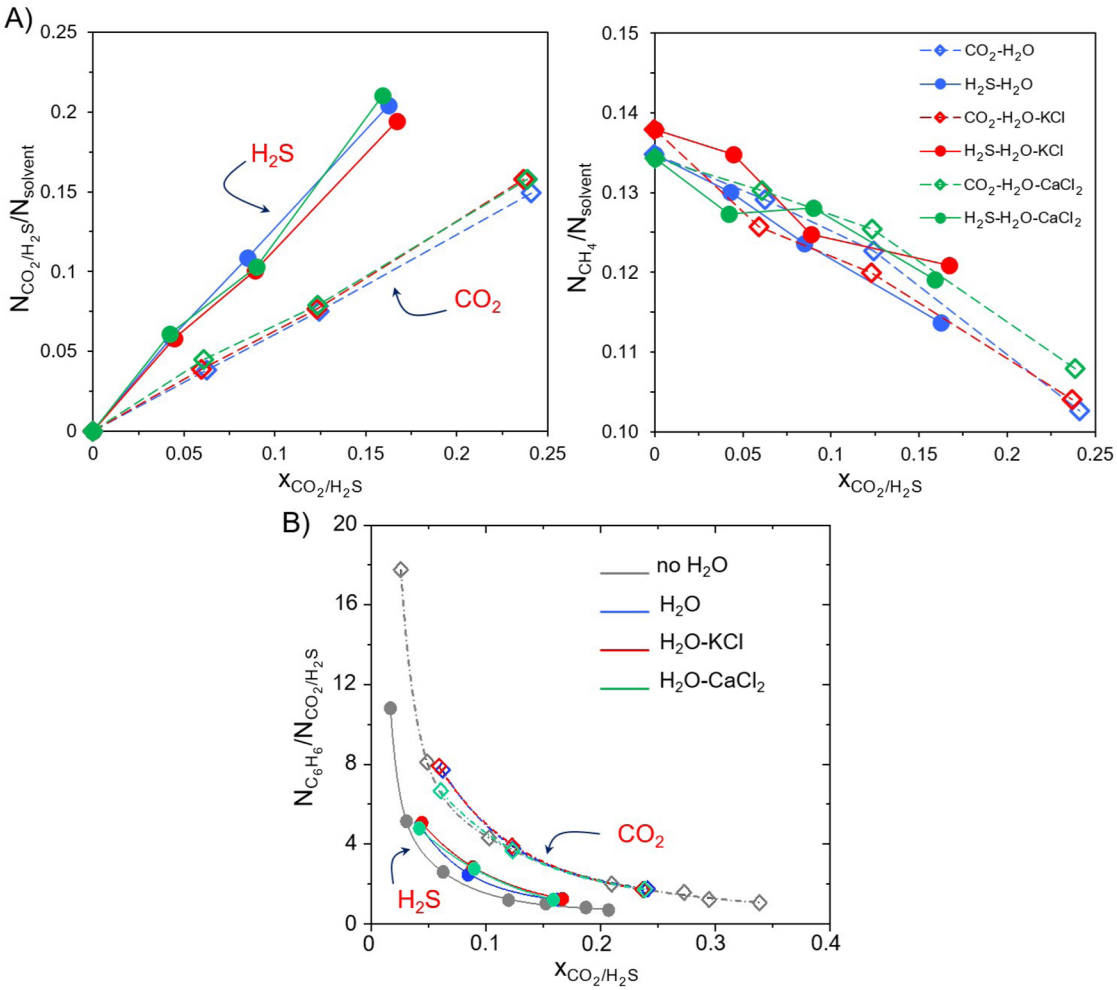

FIG. 2. (a) CO_2/H_2S (left) and CH_4 (right) solubility within the pore vs CO_2/H_2S bulk mole fractions. The results are shown for CH_4–CO_2 (empty diamonds) and CH_4–H_2S (filled circles) mixtures within the C_6H_6-filled pore saturated with H_2O (blue), H_2O–KCl (red), and H_2O–$CaCl_2$ (green) films at surfaces. (b) Number of confined C_6H_6 molecules per adsorbed CO_2/H_2S molecule vs CO_2 (empty diamonds) and H_2S (filled circles) bulk mole fractions. The results found in the C_6H_6-filled pore (gray) reported in a previous study[30] are also shown for comparison.

simulations. The external force yields a pressurized zone on the right of the porous media, within which an increase in CH_4 and CO_2 densities is observed (see Fig. S4 of the supplementary material). This is the "retentate" volume. The external field effectively imposes a density gradient across the pore, leading to a macroscopic flux in the direction of the arrow in Fig. 1. Once a density gradient is achieved, CH_4 and CO_2/H_2S molecules diffuse from the retentate to the "eluate" volume, where the fluid density is lower. Once a steady state flow is achieved and then maintained, dynamical properties can be extracted from the simulation results. Note that the transport diffusivity D_t is determined when the eternal force goes to 0, in which the structure of the pore network remains unaltered in response to the imposed pressure. Thus, it is essential to apply an external force, e.g., 0.01 kcal/(mol Å), small enough to guarantee the integrity of the fluid structure within the simulated pore.[30]

The molar flux along the X direction, J_i, was estimated by counting the number of molecule of species i (CH_4, CO_2, or H_2S) passing through a Y–Z plane at a given X location within the pore as a function of the production simulation time, t, and the cross-sectional area across which the flux moved, $A(x)$,

$$J_i = \frac{\left(N_i^+ - N_i^-\right)_x}{tA(x)}. \quad (1)$$

In Eq. (1), N_i^+ and N_i^- are the number of molecules of CH_4, CO_2, or H_2S that traveled through the plane from right to left and from left to right, respectively, as depicted in Fig. 1.

Once the flux is determined, the permeability, K, can be quantified recalling Darcy's law,[59] which exhibits a linear correlation between molar flux and pressure drop through a pore,

$$J_i = -K_i \frac{dP_i}{dx}. \quad (2)$$

The pressure drop, dP, for each species i was computed using the Peng–Robinson EOS with the density of each species in the retentate and permeate domains as inputs.[29,60] By substituting the molar flux J_i from Eq. (1), Eq. (2) can be reconstructed and integrated to obtain K,

$$K_i = \frac{1}{\Delta P \cdot t} \int_0^l \frac{\left(N_i^+ - N_i^-\right)_x dx}{A(x)}. \quad (3)$$

The cross-sectional area of one plane within the pore $A(x)$ varies along the X direction of the pore because of the surface roughness and the non-uniform distribution of C_6H_6 molecules confined in the pore. Therefore, $A(x)$ should be estimated based on the free volume available for the different components CH_4, CO_2, and H_2S. The details about the method for $A(x)$ calculation and the results for $A(x)$ as a function of pore loading are reported in Fig. S5 of the supplementary material.

In Fig. 3(a), we report the results of CO_2 and H_2S permeabilities (left and right panels, respectively) as a function of CO_2/H_2S bulk mole fraction. The results are obtained for the C_6H_6-filled pore in the presence of H_2O (blue), H_2O–KCl (red), and H_2O–$CaCl_2$ (green) films at surfaces. For comparison, we also show the results obtained for the pore filled with only C_6H_6 (gray), which were reported previously.[30] The results show that the permeability of H_2S through the C_6H_6–H_2O/brine systems is slightly larger than that of CO_2, while in the absence of water/brines, H_2S transverses the C_6H_6-filled pore (gray) much more quickly than CO_2. CO_2 permeability through the C_6H_6–H_2O/brine systems (blue, red, and green) initially decreases upon increasing CO_2 loading and subsequently increases, which is different compared to the results obtained when

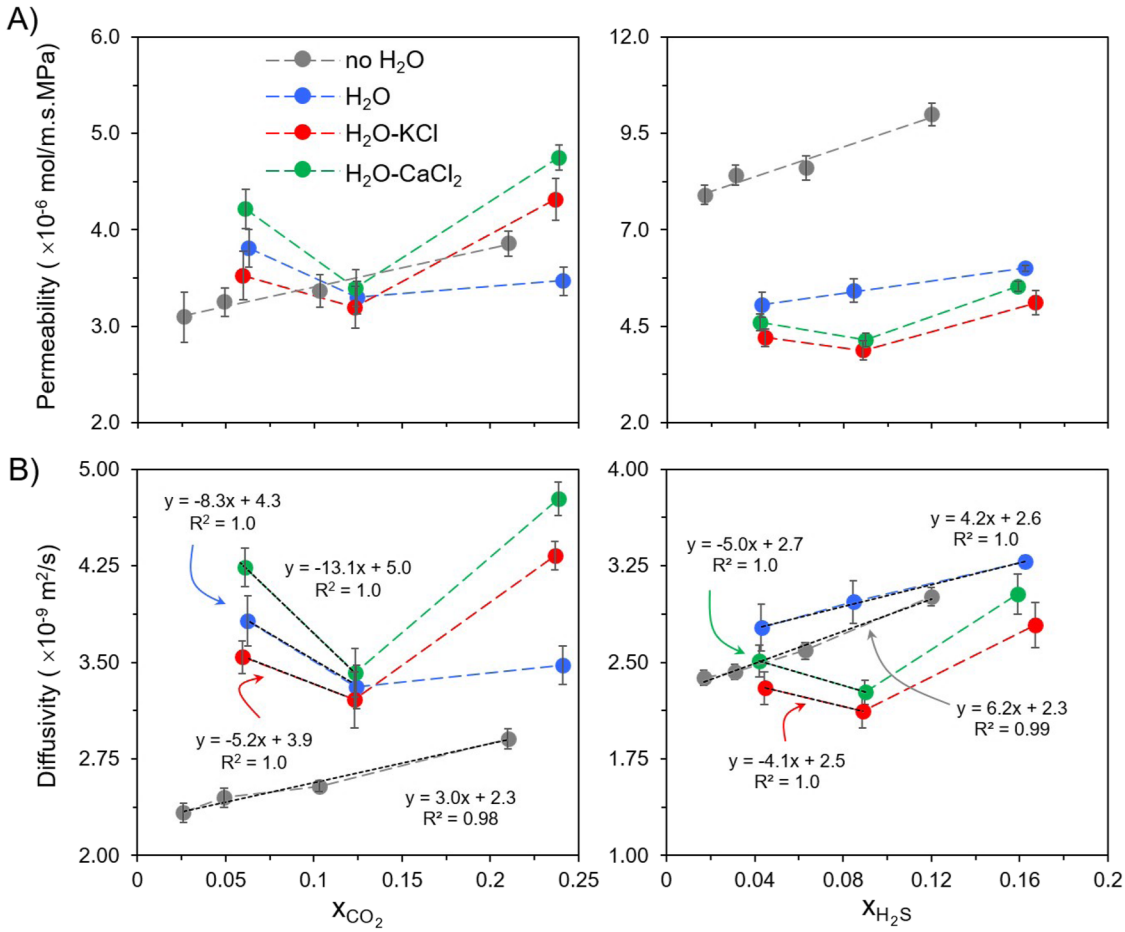

FIG. 3. Permeability (a) and transport diffusivity (b) for CO_2 (left) and H_2S (right) moving across the pore network for various systems considered. The results are shown for the pore filled with only C_6H_6 (gray), which were reported previously,[30] and the C_6H_6-filled pore in the presence of H_2O (blue), H_2O–KCl (red), and H_2O–$CaCl_2$ (green) films at the pore surfaces.

water is not present (gray). Salts affect H_2S permeability. While a monotonic increase in H_2S permeability as a function of bulk H_2S concentration is observed when pure water is present within the system (similar to what observed when no water is present—gray), in the presence of brines, as the bulk H_2S concentration increases, the permeability first decreases, reaches a minimum, and then increases.

Once the permeability is known, the transport diffusivity of CH_4, CO_2, and H_2S can be calculated as[61]

$$D_{t,i} = \frac{K_i}{S_i}, \tag{4}$$

where S_i is the solubility of species i within the pore. The solubility of species i is computed by dividing its density in the pore, ρ_i, by its partial pressure in the retentate side, p_i, using the slope of the simulated adsorption isotherms (see Fig. S6 of the supplementary material) obtained in the linear regime,[30]

$$S_i = \frac{\rho_i}{p_i}. \tag{5}$$

Solubility data for CH_4, CO_2, and H_2S are presented in Table S2 of the supplementary material. In Fig. 3(b), we report CO_2 and H_2S transport diffusivity (empty diamonds and filled circles, respectively) for all systems considered. Analogous to the results of permeability [see Fig. 3(a)], we observe non-monotonic trends for the CO_2/H_2S transport diffusivities as a function of the correspondent bulk mole fractions within the C_6H_6–brine films (red/green). The H_2S transport diffusivity through the C_6H_6–water system (blue) increases monotonically upon increasing H_2S loading, while that of CO_2 in this pore first decreases and then increases as the CO_2 bulk mole fraction increases.

Coupling of CO_2/H_2S diffusivity to C_6H_6/H_2O dynamics in confinement

For an infinitely diluted gas, the transport diffusivity approaches the self-diffusivity as commonly measured experimentally via pulsed field gradient nuclear magnetic resonance, incoherent quasi-elastic neutron scattering, or tracer zero length column.[62] In Fig. 4(a), we report CO_2 (blue) and H_2S (green) transport diffusivity through the various pores considered here at infinitely diluted conditions. The results show that the H_2O/brine films significantly enhance the transport diffusivity for CO_2 while only slightly for H_2S in the following order: no water < H_2O–KCl < H_2O < H_2O–$CaCl_2$. While the CO_2 transport diffusivity through the C_6H_6-filled pore is comparable to that of H_2S (~2.3×10^{-9} m^2/s), CO_2 diffuses faster than H_2S in the C_6H_6–H_2O/brine systems.

To understand why wetting the pore surfaces and varying the cations (K^+/Ca^{2+}) impact the transport diffusivity so strongly, we quantify the correlations between CO_2 and H_2S transport diffusivities and the dynamics of confined C_6H_6 and H_2O. We analyzed the residence autocorrelation functions $C_R(t)$ obtained for C_6H_6 molecules in the middle of the pore, between the two hydration layers, which form near the pore surfaces. $C_R(t)$ provides an estimate for how long C_6H_6 molecules remain in the identified region.[63] We then fitted $C_R(t)$ to extract the decay times—the larger the decay time, the longer the C_6H_6 molecules remain in the middle region of the pore. Although some previous studies suggested to fit autocorrelation functions using single exponentials,[64–66] our analysis did not provide satisfactory agreement. It is, in fact, known that a single exponential function might not fully describe all dynamical properties,[67,68] especially for strongly coupled systems.[69] We achieved satisfactory fitting using the double exponential function $C_R(t)(C_6H_6) = 0.4e^{-t/\tau 1} + 0.6e^{-t/\tau 2}$, with a coefficient of determination $R^2 \sim 0.99$. Our analysis revealed that the values of the fitting parameters τ_1 and τ_2 increase in the following order: H_2O–$CaCl_2$ ~ H_2O < H_2O–KCl < no water, which corresponds to the decrease order of CO_2/H_2S

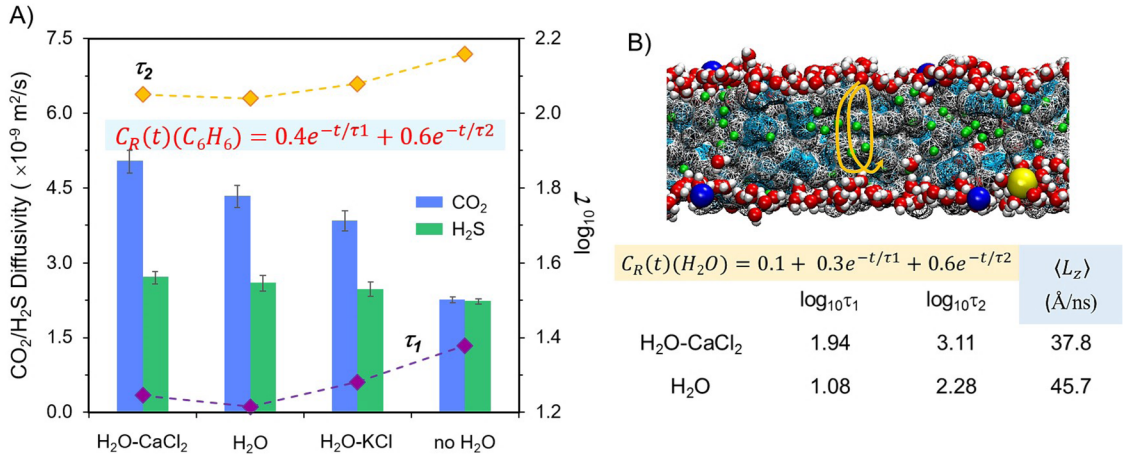

FIG. 4. (a) Correlation between CO_2/H_2S diffusivity at infinitely dilute conditions (blue/green, respectively) and the time constants for double exponential fitting for the residence autocorrelation function $C_R(t)$ of C_6H_6 confined in various pores considered. (b) Time constants for double exponential fitting for $C_R(t)$ of confined H_2O and path length of H_2O molecules moving between two hydration layers within the pore (as shown in the top panel, yellow line). The results are shown for the C_6H_6-filled pore in the presence of H_2O and H_2O–$CaCl_2$ films.

transport diffusivity [see Fig. 4(a)]. Analyzing the distribution of C_6H_6 molecules within layers alongside the SiO_2 surfaces (see Fig. S7 of the supplementary material), we conclude that the H_2O/brine film at the C_6H_6-filled pore surfaces distorts the C_6H_6 structure in the middle region of the pores, both speeding up C_6H_6 dynamics and enhancing CO_2/H_2S diffusion.

The CO_2/H_2S transport diffusivity found for systems containing H_2O–$CaCl_2$ layers is larger than that obtained for the C_6H_6–H_2O system, although the τ_1 and τ_2 values for $C_R(t)$ obtained for C_6H_6 molecules in both cases are similar. This suggests that other factors may also manipulate the CO_2/H_2S diffusion. To gain further insights, we analyze $C_R(t)$ for H_2O molecules adsorbed at the pore surfaces [see Fig. 4(b), top] for the C_6H_6-filled pore saturated with H_2O/H_2O–$CaCl_2$, and we fit the results with the double exponential function $C_R(t)(H_2O) = 0.1 + 0.3e^{-t/\tau 1} + 0.6e^{-t/\tau 2}$. For brevity (see Fig. S8 of the supplementary material), we only fit the data from the bottom surfaces. The results suggest that H_2O is more mobile when Ca^{2+} and Cl^- ions are not present. Analyzing the walking path lengths in the Z direction confirms that H_2O molecules travel back and forth between the two hydration layers more frequently when $CaCl_2$ is not present. We conclude that the back-and-forth movement of H_2O [the yellow line in Fig. 4(b), top] between the pore surfaces might cause "traffic," which hinders CO_2 and H_2S diffusion throughout the pore networks.

CH_4 transport

In Fig. 5(a), we present the CH_4 permeabilities for CH_4–CO_2 and CH_4–H_2S mixtures (left and right panels, respectively) upon loading CO_2/H_2S. The results are obtained for the C_6H_6–H_2O (blue), H_2O–KCl (red), and H_2O–$CaCl_2$ (green) systems, as well as for the pore with no water (gray), from prior work.[30] We observe analogous trends for CH_4 permeability as a function of bulk CO_2/H_2S concentrations for both mixtures as the ones obtained for CO_2 and H_2S permeability, as in Fig. 3(a).

In Fig. 5(b), it is shown that the CH_4 flux for both mixtures traveling through the C_6H_6–brine systems initially decreases upon increasing CO_2/H_2S loading and subsequently increases (red and green, respectively). This indicates that CO_2 and H_2S function as barriers, impeding CH_4 movement through the pore at low CO_2/H_2S bulk mole fractions. CO_2 seems to hinder the CH_4 migration through the C_6H_6–H_2O system (empty diamonds, blue) at a low CO_2 bulk mole fraction as well, while H_2S facilitates CH_4 transport (filled circles, blue) (similar to what observed when no water is present—gray).[30] In addition, the results show a linear relation between the molar flux of CH_4 and the CO_2/H_2S bulk mole fractions in the low concentration regime [see Fig. 5(b), yellow area].

One fundamental question stems from this quantitative observation: how wetting H_2O/brine at the C_6H_6-filled pore surfaces significantly alters the transport behavior of CO_2 and H_2S, leading to speeding up or hampering the CH_4 transport through the pores at low bulk CO_2/H_2S concentrations (x_{CO_2/H_2S})?

Adsorption energies

To address the above question, we calculated the adsorption energy of one molecule for each C_6H_6, H_2S, CO_2, and CH_4 within the pores containing H_2O/brine films and filled with C_6H_6 and

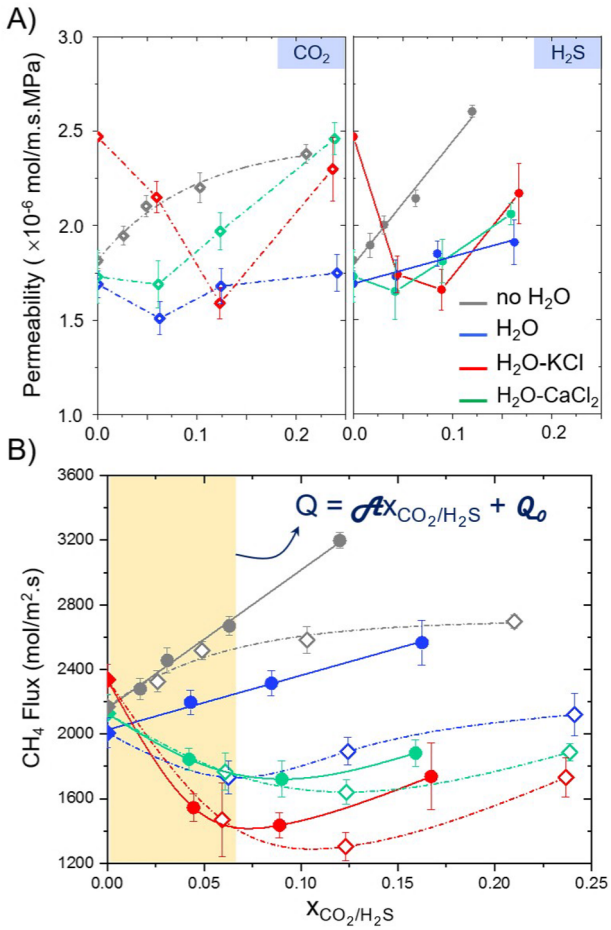

FIG. 5. Permeability (a) and molar flux (b) of CH_4 from CH_4–CO_2 (empty diamonds, left) and CH_4–H_2S (filled circles, right) mixtures across the pore network upon loading CO_2/H_2S. The results are shown for the pore filled with only C_6H_6 (gray) and the C_6H_6-filled pore in the presence of H_2O (blue), H_2O–KCl (red), and H_2O–$CaCl_2$ (green) films at the pore surfaces.

CH_4 molecules. We employed the two-box procedure suggested by Heinz.[70] The adsorption energy ΔE_{ads} is obtained as the difference between the total energy of the two systems, with pore, E_1, and the bulk, E_2,

$$\Delta E_{ads} = \langle E_1 \rangle - \langle E_2 \rangle. \quad (6)$$

We ran 10–20 simulations for each configuration to obtain average values for both $\langle E_1 \rangle$ and $\langle E_2 \rangle$. In Fig. 6, top panel, we report the adsorption energy of C_6H_6 (gray), H_2S (red), CO_2 (blue), and CH_4 (green), within the C_6H_6–H_2O/brine porous systems. Prior results for the pore with C_6H_6 and no water are also shown.[30] The H_2O/brine films at the pore surfaces remarkably reduce the attractive interactions between CO_2/H_2S and the pores. Specifically, H_2S is more strongly adsorbed in the pore as the system composition

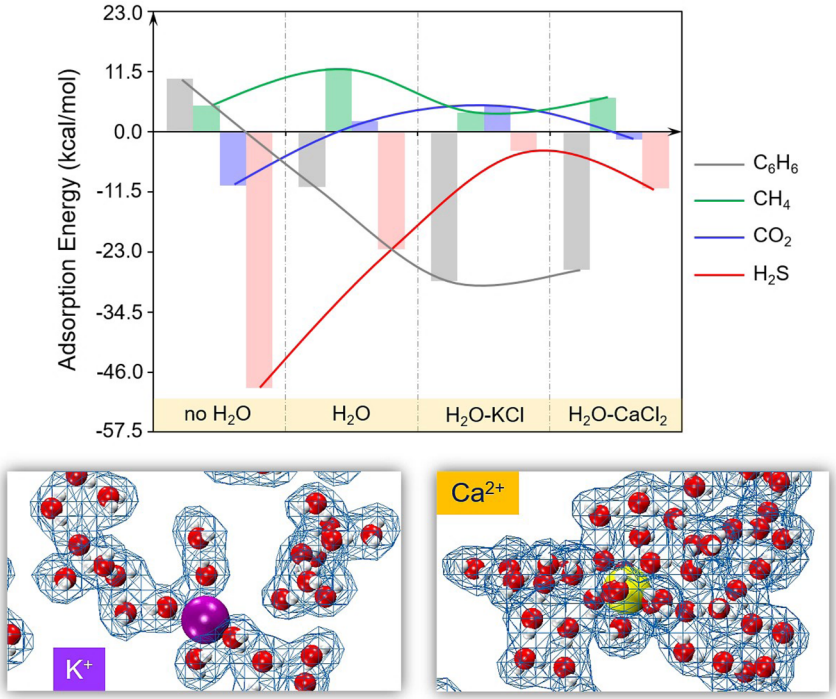

FIG. 6. Top: Adsorption energies of one C_6H_6 (gray), H_2S (red), CO_2 (blue), and CH_4 (green) molecule in the silica pore including C_6H_6, H_2O/brine films, and CH_4 and in the bulk regions consisting of only CH_4. The results are shown for the pore filled with only C_6H_6 and the C_6H_6-filled pore saturated with H_2O/brine films at surfaces. Bottom: Top view of the distributions of H_2O molecules and K^+/Ca^{2+} cations (purple/yellow spheres in the left/right panel, respectively) adsorbed at the bottom SiO_2 surfaces. The volumetric maps for H_2O density are also shown as blue wireframes.

changes in the following order: H_2O–KCl < H_2O–$CaCl_2$ < H_2O < no H_2O. CO_2 is also more strongly adsorbed in the C_6H_6-filled pore (−10.38 kcal/mol)[30] than in the pores containing H_2O/brine films (−1.61 kcal/mol, 2.08 kcal/mol, and 5.07 kcal/mol, respectively). On the other hand, the presence of H_2O in the C_6H_6-filled pore enhances the adsorption energy of C_6H_6 significantly.[30] The latter observation is possibly due to the fact that the C_6H_6–H_2O interaction energy (−3.16 kcal/mol)[71] is more attractive than those of C_6H_6–C_6H_6 dimers (−1.81 kcal/mol to −2.78 kcal/mol).[72,73] C_6H_6 is even more strongly adsorbed when K^+/Ca^{2+} and Cl^- ions are present.

Varying the type of cation (K^+ and Ca^{2+}) strongly impacts the adsorption energy of C_6H_6 in the order Ca^{2+} (−26.52 kcal/mol) < K^+ (−28.60 kcal/mol), as well as those for CO_2/H_2S (blue/red) (see Fig. 6, top panel). Numerous *ab initio* studies[74,75] have shown that a Ca^{2+} ion binds to a C_6H_6 ring (−71.57 kcal/mol) along the π plane much more strongly than a K^+ ion does (−16.64 kcal/mol). However, in aqueous solutions, the order is reversed, which is confirmed by Rimmen *et al.*[76] They investigated how Ca^{2+} and K^+ in aqueous solutions affect the interactions between surfaces covered by self-assembled monolayers terminated with C_6H_6 using x-ray photoelectron spectroscopy (XPS).[76] Their results showed that Ca^{2+} does not bind as strongly to the C_6H_6 layers as K^+ does[76] likely due to the fact that Ca^{2+} interacts with H_2O more strongly than K^+. Ca^{2+} is unlikely to associate with C_6H_6 rings because of its strong hydration, while aqueous K^+ can interact with up to three C_6H_6 rings, in good agreement with *ab initio* studies.[77] This possibly accounts for the slower dynamic of confined C_6H_6 in the H_2O–KCl systems than those observed in C_6H_6–H_2O and H_2O–$CaCl_2$ systems [see Fig. 4(a)]. Consistent with the experimental study, our simulation results show that H_2O molecules at the pore surfaces do not fully cover K^+ ions, allowing them to be exposed to C_6H_6, while Ca^{2+} ions are thoroughly hydrated by H_2O (see Fig. 6, bottom left and right panels). We also quantified the volumetric maps for H_2O density (blue wireframes in Fig. 6, bottom). Those structural observations could explain why the adsorption energy of C_6H_6 in the C_6H_6-filled pore containing brine films increases in the following order: Ca^{2+} < K^+. These data seem consistent with Hofmeister's series.[78,79]

Surprisingly, we note that CO_2/H_2S expedites CH_4 transport through the C_6H_6-filled pore systems when CO_2/H_2S is preferentially adsorbed compared to C_6H_6 (e.g., CO_2/H_2S in the C_6H_6-filled pore or H_2S in the C_6H_6–H_2O pore). However, our results show that CO_2/H_2S would hinder the CH_4 migration across the pore at low CO_2/H_2S bulk mole fractions when CO_2/H_2S is less attracted to the pore than C_6H_6; this is particularly evident in the systems containing brine films.

Predictive phenomenological models

We recall that the molar flux of CH_4 through the pore increases or decreases linearly with the CO_2/H_2S bulk mole fraction at low x_{CO_2/H_2S} regimes [see Fig. 5(b), yellow area]. This can be described as

$$Q_{CH_4} = \mathscr{A} x_{CO_2/H_2S} + Q_0, \tag{7}$$

where Q_0 is the molar flux of CH_4 when $x_{CO_2/H_2S} = 0$.

Because the results discussed above suggest that the enhancement/hindrance for CH_4 transport strongly depends on whether CO_2/H_2S is more or less attracted to the pore network than C_6H_6, we seek a relationship between CH_4 molar flux and the adsorption energy of C_6H_6, H_2S, CO_2, and CH_4 for the pore considered in this study. Plotting the slope of the linear correlation between CH_4 molar flux and the CO_2/H_2S bulk mole fraction at low x_{CO_2/H_2S}, $\mathscr{A}$, vs the difference between the adsorption energy of C_6H_6 and that of CO_2 (left) and H_2S (right) [$\Delta E(C_6H_6–CO_2)$ and $\Delta E(C_6H_6–H_2S)$], we observe the exponential relationship [see Fig. 7 (top panels)]

$$\mathscr{A} \propto \alpha^{\Delta E(C_6H_6-CO_2/H_2S)}. \tag{8}$$

We then examine the correlation between the CH_4 molar flux and its adsorption energy when CO_2 and H_2S are not present. It is found that the CH_4 molar flux decreases exponentially with the increase in its positive adsorption energy [see Fig. 7 (bottom panel), in which each data point represents the result obtained for the C_6H_6-filled pore and the pore filled with C_6H_6 and H_2O/brine films at surfaces],

$$Q_0 \propto c^{E(CH_4)}. \tag{9}$$

Substituting Eqs. (8) and (9) within the linear relation between the CH_4 molar flux and the CO_2/H_2S bulk mole fraction [Eq. (7)], we find that the CH_4 molar flux through the pore networks considered

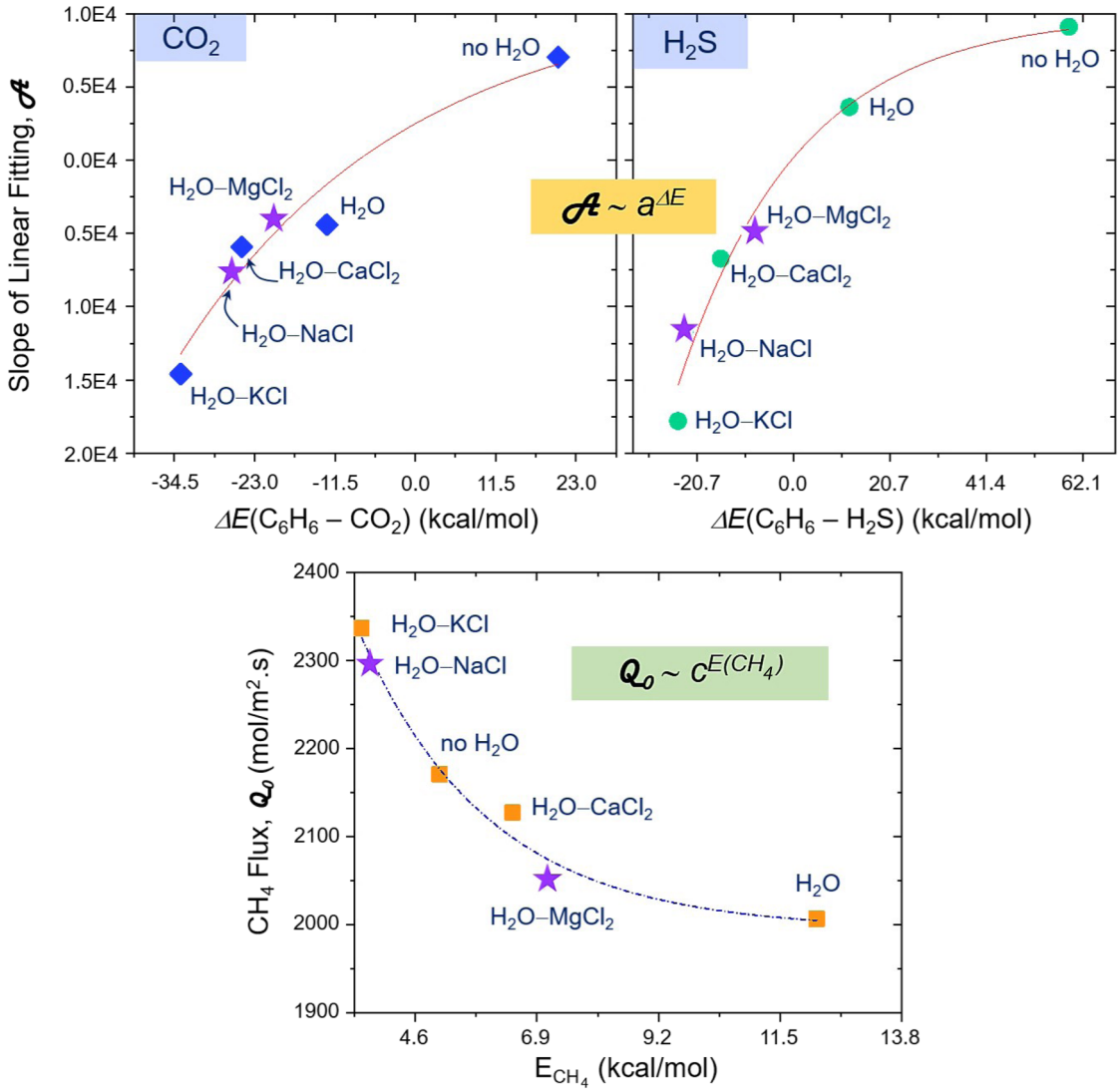

FIG. 7. Top: Relation between the slope of linear fitting, $\mathscr{A}$, for the methane flux at low CO_2/H_2S bulk mole fractions and the difference between the adsorption energy of C_6H_6 and that of CO_2/H_2S (left/right panel, respectively). Bottom: Relation between the methane flux (no CO_2/H_2S present in the flow) and the adsorption energy of methane. Each data point represents the result obtained for C_6H_6–H_2O, H_2O–KCl, and H_2O–$CaCl_2$ systems, as well as for the pore with no water.

here is a function of the adsorption energy of C_6H_6, CO_2, H_2S, and CH_4, as quantified by

$$Q_{CH_4} \propto \alpha^{\Delta E(C_6H_6-CO_2/H_2S}x_{CO_2/H_2S} + c^{E(CH_4)}. \quad (10)$$

Although Eq. (10) is only applicable at low x_{CO_2/H_2S}, it seems relevant for shale gas production, as the CO_2/H_2S concentration in shale gas is generally less than 0.08–0.10.[80,81]

To test applicability and reliability of our phenomenological model, we constructed additional simulation systems in which new cations, e.g., sodium and magnesium (Na^+ and Mg^{2+}), were added to the pore pre-filled with C_6H_6, H_2O, and Cl^- anions. The results show that the correlation between CH_4 molar flux and the adsorption energy of C_6H_6, H_2S, CO_2, and CH_4 in the presence of Na^+/Mg^{2+} follows the exponential relationship described in Eqs. (8) and (9) [see Figs. 7(a) and 7(b), purple stars]. This suggests that the interaction energies for C_6H_6, H_2S, CO_2, and CH_4 in each pore network could provide a quantitative estimate for the molar flux of CH_4 at low concentrations of the second component while saving significant amounts of computational resources.

CONCLUSIONS

In this study, we investigate the impact of water/brines (either KCl or $CaCl_2$) on adsorption and transport of gases containing CH_4 and either CO_2 or H_2S in amorphous slit-shaped silica nanopores filled with benzene. The results show that the presence of water/brines in the porous systems remarkably affects the adsorption energies of all species. This leads to the significantly reduced amount of adsorbed H_2S, CO_2, and CH_4 in the pores and to strong effects on their transport mechanisms. We observe a coupling between CO_2/H_2S transport diffusivity of CO_2/H_2S at infinitely diluted conditions and the dynamics of confined benzene and water mediated by salt-specific effects. CO_2 and H_2S play the roles of either vehicle-like carriers or barriers to the CH_4 transport depending on whether CO_2/H_2S is more or less strongly adsorbed in the pores than benzene; the preferential adsorption energies are found to be strongly affected by the presence of water and brines. We found an exponential correlation between the CH_4 molar flux and the adsorption energies of CH_4, CO_2/H_2S, and benzene, suggesting that shale gas transport properties could be predicted once adsorption energy data of all components are available. Because aqueous electrolytes are ubiquitous and because Na^+, K^+, Ca^{2+}, and Mg^{2+} are the most common alkali and alkaline earth cations, our results provide better understanding, at the molecular level, regarding transport phenomena that take place during shale gas exploration and production, geologic CO_2 storage, and EOR processes.

SUPPLEMENTARY MATERIAL

See the supplementary material for the full details of properties of interests such as adsorption isotherms, the amount of displaced benzene, density profiles, cross-sectional area, in-plane surface density distributions, and residence autocorrelation functions.

ACKNOWLEDGMENTS

Generous allocations of computing time were provided by ARCHER, the UK National Supercomputing Service (http://www.archer.ac.uk), via our membership in the UK HEC Materials Chemistry Consortium, which is funded by the EPSRC (Grant Nos. EP/L000202 and EP/R029431), the University College London Research Computing Platforms Support (Myriad), and the National Energy Research Scientific Computing Center (NERSC) at Lawrence Berkeley National Laboratory. The NERSC is supported by the DOE, Office of Science, under Contract No. DE-AC02-05CH11231. This work was supported, in part, by the Science4CleanEnergy European Research Infrastructure Consortium funded by the European Union's Horizon 2020 research and innovation program under Grant Agreement No. 764810 (S4CE).

DATA AVAILABILITY

The data that support the findings of this study are available from the corresponding author upon reasonable request.

REFERENCES

[1] I. C. Bourg and J. B. Ajo-Franklin, "Clay, water, and salt: Controls on the permeability of fine-grained sedimentary rocks," Acc. Chem. Res. **50**(9), 2067–2074 (2017).
[2] IPCC, *IPCC Special Report on Carbon Dioxide Capture and Storage* (Cambridge University Press, Cambridge, UK, 2005).
[3] B. Smit, J. R. Reimer, C. M. Oldenburg, and I. C. Bourg, *Introduction to Carbon Capture and Sequestration* (Imperial College Press, London, 2014).
[4] I. C. Bourg, "Sealing shales versus brittle shales: A sharp threshold in the material properties and energy technology uses of fine-grained sedimentary rocks," Environ. Sci. Technol. Lett. **2**(10), 255–259 (2015).
[5] *Horn River Basin Unconventional Shale Gas Play Atlas* (BC Oil and Gas Commission, 2014).
[6] R. H. Weiland and N. A. Hatcher, "Overcome challenges in treating shale gases," Hydrocarbon Process. **91**(1), 45–48 (2012).
[7] C. L. Cipolla, E. P. Lolon, J. C. Erdle, and B. Rubin, "Reservoir modeling in shale-gas reservoirs," SPE Reservoir Eval. Eng. **13**(4), 638–653 (2010).
[8] B. Tilley, S. McLellan, S. Hiebert, B. Quartero, B. Veilleux, and K. Muehlenbachs, "Gas isotope reversals in fractured gas reservoirs of the Western Canadian Foothills: Mature shale gases in disguise," AAPG Bull. **95**(8), 1399–1422 (2011).
[9] M. Parker, D. Buller, E. Petre, and D. H. Dreher, "Haynesville shale-petrophysical evaluation," in *SPE Rocky Mountain Petroleum Technology Conference*, Denver, CO, 14-16 April 2009 (Society of Petroleum Engineers, 2009).
[10] R. N. Maddox and J. Morgan, *Gas Conditioning and Processing: Gas Treating and Sulfur Recovery*, Campbell Petroleum Series Vol. 4 (John M. Campbell and Company, Norman, OK, 2006).
[11] A. Hofmann, W. van Strien, and R. Malekzadeh, in *Improving the Efficiency of H2S Mitigation in Middle East Oil and Gas Fields* (Society of Petroleum Engineers, Abu Dhabi, UAE, 2017).
[12] C. Khan, R. Amin, and G. Madden, "Effects of CO_2 and acid gas injection on enhanced gas recovery and storage," J. Pet. Explor. Prod. Technol. **3**(1), 55–60 (2013).
[13] S. O. Snaebjornsdottir, E. H. Oelkers, K. Mesfin, E. S. Aradottir, K. Dideriksen, I. Gunnarsson, E. Gunnlaugsson, J. M. Matter, M. Stute, and S. R. Gislason, "The chemistry and saturation states of subsurface fluids during the *in situ* mineralisation of CO_2 and H_2S at the CarbFix site in SW-Iceland," Int. J. Greenhouse Gas Control **58**, 87–102 (2017).
[14] B. Zou, C. S. McCool, D. W. Green, and G. P. Willhite, "A study of the chemical interactions between brine solutions and dolomite," SPE Reservoir Eval. Eng. **3**(3), 209–215 (2000).

[15]G. M. Bowers, H. T. Schaef, J. S. Loring, D. W. Hoyt, S. D. Burton, E. D. Walter, and R. J. Kirkpatrick, "Role of cations in CO_2 adsorption, dynamics, and hydration in smectite clays under in situ supercritical CO_2 conditions," J. Phys. Chem. C **121**(1), 577–592 (2017).
[16]N. Loganathan, A. O. Yazaydin, G. M. Bowers, B. F. Ngouana-Wakou, A. G. Kalinichev, and R. J. Kirkpatrick, "Role of cations in the methane/carbon dioxide partitioning in nano- and mesopores of illite using constant reservoir composition molecular dynamics simulation," J. Phys. Chem. C **124**(4), 2490–2500 (2020).
[17]J. A. Greathouse, R. T. Cygan, J. T. Fredrich, and G. R. Jerauld, "Adsorption of aqueous crude oil components on the basal surfaces of clay minerals: Molecular simulations including salinity and temperature effects," J. Phys. Chem. C **121**(41), 22773–22786 (2017).
[18]A. G. Ilgen, J. E. Heath, I. Y. Akkutlu, L. T. Bryndzia, D. R. Cole, Y. K. Kharaka, T. J. Kneafsey, K. L. Milliken, L. J. Pyrak-Nolte, and R. Suarez-Rivera, "Shales at all scales: Exploring coupled processes in mudrocks," Earth-Sci. Rev. **166**, 132–152 (2017).
[19]T. Manzocchi, C. Childs, and J. J. Walsh, "Faults and fault properties in hydrocarbon flow models," Geofluids **10**(1-2), 94–113 (2010).
[20]J. R. Meyer, B. L. Parker, and J. A. Cherry, "Characteristics of high resolution hydraulic head profiles and vertical gradients in fractured sedimentary rocks," J. Hydrol. **517**, 493–507 (2014).
[21]M. Mazurek, P. Alt-Epping, A. Bath, T. Gimmi, H. Niklaus Waber, S. Buschaert, P. D. Cannière, M. D. Craen, A. Gautschi, S. Savoye *et al.*, "Natural tracer profiles across argillaceous formations," Appl. Geochem. **26**(7), 1035–1064 (2011).
[22]J. W. Cosgrove, "Hydraulic fracturing during the formation and deformation of a basin: A factor in the dewatering of low-permeability sediments," AAPG Bull. **85**(4), 737–748 (2001).
[23]S. Iglauer, A. Z. Al-Yaseri, and D. Wolff-Boenisch, "Basalt-CO_2-brine wettability at storage conditions in basaltic formations," Int. J. Greenhouse Gas Control **102**, 103148 (2020).
[24]B. Sun, B. D. Stewart, A. N. Kucharski, and P. M. Kekenes-Huskey, "Thermodynamics of cation binding to the sarcoendoplasmic reticulum calcium ATPase pump and impacts on enzyme function," J. Chem. Theory Comput. **15**(4), 2692–2705 (2019).
[25]W. C. Jolin, R. Goyetche, K. Carter, J. Medina, D. Vasudevan, and A. A. MacKay, "Predicting organic cation sorption coefficients: Accounting for competition from sorbed inorganic cations using a simple probe molecule," Environ. Sci. Technol. **51**(11), 6193–6201 (2017).
[26]H. Frentrup, C. Avendaño, M. Horsch, A. Salih, and E. A. Müller, "Transport diffusivities of fluids in nanopores by non-equilibrium molecular dynamics simulation," Mol. Simul. **38**(7), 540–553 (2012).
[27]S. He, J. C. Palmer, and G. Qin, "A non-equilibrium molecular dynamics study of methane transport in clay nano-pores," Microporous Mesoporous Mater. **249**, 88–96 (2017).
[28]J. Muscatello, F. Jaeger, O. K. Matar, and E. A. Müller, "Optimizing water transport through graphene-based membranes: Insights from nonequilibrium molecular dynamics," ACS Appl. Mater. Interfaces **8**(19), 12330–12336 (2016).
[29]A. Phan and A. Striolo, "Methane transport through hierarchical silica micro-mesoporous materials: From non-equilibrium atomistic simulations to phenomenological correlations," Microporous Mesoporous Mater. **288**, 109559 (2019).
[30]A. Phan and A. Striolo, "Evidence of facilitated transport in crowded nanopores," J. Phys. Chem. Lett. **11**(5), 1814–1821 (2020).
[31]P. Ugliengo, M. Sodupe, F. Musso, I. J. Bush, R. Orlando, and R. Dovesi, "Realistic models of hydroxylated amorphous silica surfaces and MCM-41 mesoporous material simulated by large-scale periodic B3LYP calculations," Adv. Mater. **20**(23), 4579–4583 (2008).
[32]L. Ma, A.-L. Fauchille, P. J. Dowey, F. Figueroa Pilz, L. Courtois, K. G. Taylor, and P. D. Lee, "Correlative multi-scale imaging of shales: A review and future perspectives," Geol. Soc. Spec. Publ. **454**, 175–199 (2017).
[33]M. Arif, F. Jones, A. Barifcani, and S. Iglauer, "Influence of surface chemistry on interfacial properties of low to high rank coal seams," Fuel **194**, 211–221 (2017).
[34]H. Takahashi, D. Suzuoka, and A. Morita, "Why is benzene soluble in water? Role of OH/π interaction in solvation," J. Chem. Theory Comput. **11**(3), 1181–1194 (2015).
[35]M. Arif, M. Lebedev, A. Barifcani, and S. Iglauer, "Influence of shale-total organic content on CO_2 geo-storage potential," Geophys. Res. Lett. **44**(17), 8769–8775, https://doi.org/10.1002/2017gl073532 (2017).
[36]R. T. Cygan, J.-J. Liang, and A. G. Kalinichev, "Molecular models of hydroxide, oxyhydroxide, and clay phases and the development of a general force field," J. Phys. Chem. B **108**(4), 1255–1266 (2004).
[37]J. J. Potoff and J. I. Siepmann, "Vapor-liquid equilibria of mixtures containing alkanes, carbon dioxide, and nitrogen," AIChE J. **47**(7), 1676–1682 (2001).
[38]M. S. Shah, M. Tsapatsis, and J. I. Siepmann, "Development of the transferable potentials for phase equilibria model for hydrogen sulfide," J. Phys. Chem. B **119**(23), 7041–7052 (2015).
[39]M. G. Martin and J. I. Siepmann, "Transferable potentials for phase equilibria. 1. United-atom description of *n*-alkanes," J. Phys. Chem. B **102**(14), 2569–2577 (1998).
[40]P. Procacci, "PrimaDORAC: A free web interface for the assignment of partial charges, chemical topology, and bonded parameters in organic or drug molecules," J. Chem. Inf. Model. **57**(6), 1240–1245 (2017).
[41]L. X. Dang, "Mechanism and thermodynamics of ion selectivity in aqueous-solutions of 18-crown-6 ether: A molecular-dynamics study," J. Am. Chem. Soc. **117**(26), 6954–6960 (1995).
[42]M. Predota, Z. Zhang, P. Fenter, D. J. Wesolowski, and P. T. Cummings, "Electric double layer at the rutile (110) surface. 2. Adsorption of ions from molecular dynamics and X-ray experiments," J. Phys. Chem. B **108**(32), 12061–12072 (2004).
[43]H. J. C. Berendsen, J. R. Grigera, and T. P. Straatsma, "The missing term in effective pair potentials," J. Phys. Chem. **91**(24), 6269–6271 (1987).
[44]D. Vassetti, M. Pagliai, and P. Procacci, "Assessment of GAFF2 and OPLS-AA general force fields in combination with the water models TIP3P, SPCE, and OPC3 for the solvation free energy of druglike organic molecules," J. Chem. Theory Comput. **15**(3), 1983–1995 (2019).
[45]S. Mamatkulov, M. Fyta, and R. R. Netz, "Force fields for divalent cations based on single-ion and ion-pair properties," J. Chem. Phys. **138**(2), 024505 (2013).
[46]M. P. Allen and D. J. Tildesley, *Computer Simulation of Liquids* (Oxford University Press, Oxford, UK, 2004).
[47]J. W. Eastwood, R. W. Hockney, and D. N. Lawrence, "P3M3DP—The 3-dimensional periodic particle-particle-particle-mesh program," Comput. Phys. Commun. **19**(2), 215–261 (1980).
[48]R. Privat, F. Mutelet, and J.-N. Jaubert, "Addition of the hydrogen sulfide group to the PPR78 model (predictive 1978, Peng–Robinson equation of state with temperature dependent k_{ij} calculated through a group contribution method)," Ind. Eng. Chem. Res. **47**(24), 10041–10052 (2008).
[49]K. Kato, K. Nagahama, and M. Hirata, "Generalized interaction parameters for the Peng–Robinson equation of state: Carbon dioxide *n*-paraffin binary systems," Fluid Phase Equilib. **7**, 219–231 (1981).
[50]J. J. Carroll and A. E. Mather, "A generalized correlation for the Peng-Robinson interaction coefficients for paraffin hydrogen-sulfide binary-systems," Fluid Phase Equilib. **105**(2), 221–228 (1995).
[51]S. Plimpton, "Fast parallel algorithms for short-range molecular-dynamics," J. Comput. Phys. **117**(1), 1–19 (1995).
[52]R. W. Hockney, S. P. Goel, and J. W. Eastwood, "Quiet high-resolution computer models of a plasma," J. Comput. Phys. **14**(2), 148–158 (1974).
[53]S. Nosé, "A molecular-dynamics method for simulations in the canonical ensemble," Mol. Phys. **52**(2), 255–268 (1984).
[54]W. G. Hoover, "Canonical dynamics: Equilibrium phase-space distributions," Phys. Rev. A **31**(3), 1695–1697 (1985).
[55]S. Chempath, R. Krishna, and R. Q. Snurr, "Nonequilibrium molecular dynamics simulations of diffusion of binary mixtures containing short *n*-alkanes in faujasite," J. Phys. Chem. B **108**(35), 13481–13491 (2004).
[56]P. H. Hünenberger, "Thermostat algorithms for molecular dynamics simulations," Adv. Polym. Sci. **173**, 105–147 (2005).
[57]M. Bonomi, D. Branduardi, G. Bussi, C. Camilloni, D. Provasi, P. Raiteri, D. Donadio, F. Marinelli, F. Pietrucci, R. A. Broglia *et al.*, "PLUMED: A portable

plugin for free-energy calculations with molecular dynamics," Comput. Phys. Commun. **180**(10), 1961–1972 (2009).
[58]M. Bonomi, G. Bussi, C. Camilloni, G. A. Tribello, P. Banas, A. Barducci, M. Bernetti, P. G. Bolhuis, S. Bottaro, D. Branduardi *et al.*, "Promoting transparency and reproducibility in enhanced molecular simulations," Nat. Methods **16**(8), 670–673 (2019).
[59]R. M. Roque-Malherbe, *Adsorption and Diffusion in Nanoporous Materials* (CRC Press, 2007).
[60]A. Phan, D. R. Cole, R. G. Weiss, J. Dzubiella, and A. Striolo, "Confined water determines transport properties of guest molecules in narrow pores," ACS Nano **10**(8), 7646–7656 (2016).
[61]J. Liu and J. Jiang, "Molecular design of microporous polymer membranes for the upgrading of natural gas," J. Phys. Chem. C **123**(11), 6607–6615 (2019).
[62]J. Kärger, D. M. Ruthven, and D. N. Theodorou, *Diffusion in Nanoporous Materials* (John Wiley & Sons, Weinheim, 2012).
[63]A. Phan, D. R. Cole, and A. Striolo, "Preferential adsorption from liquid water-ethanol mixtures in alumina pores," Langmuir **30**(27), 8066–8077 (2014).
[64]I. Kwon, J. D. Kress, and L. A. Collins, "Tight-binding models for hot dense hydrogen," Phys. Rev. B **50**(13), 9118–9123 (1994).
[65]D. A. Horner, F. Lambert, J. D. Kress, and L. A. Collins, "Transport properties of lithium hydride from quantum molecular dynamics and orbital-free molecular dynamics," Phys. Rev. B **80**(2), 024305 (2009).
[66]J. D. Kress, J. S. Cohen, D. P. Kilcrease, D. A. Horner, and L. A. Collins, "Quantum molecular dynamics simulations of transport properties in liquid and dense-plasma plutonium," Phys. Rev. E **83**(2), 026404 (2011).
[67]P. Setny, R. Baron, P. Michael Kekenes-Huskey, J. A. McCammon, and J. Dzubiella, "Solvent fluctuations in hydrophobic cavity-ligand binding kinetics," Proc. Natl. Acad. Sci. U. S. A. **110**(4), 1197–1202 (2013).
[68]A. Ali, T. T. B. Le, A. Striolo, and D. R. Cole, "Salt effects on the structure and dynamics of interfacial water on calcite probed by equilibrium molecular dynamics simulations," J. Phys. Chem. C **124**(45), 24822–24836 (2020).
[69]J. F. Danel, L. Kazandjian, and G. Zerah, "Numerical convergence of the self-diffusion coefficient and viscosity obtained with Thomas-Fermi-Dirac molecular dynamics," Phys. Rev. E **85**(6), 066701 (2012).
[70]H. Heinz, "Computational screening of biomolecular adsorption and self-assembly on nanoscale surfaces," J. Comput. Chem. **31**(7), 1564–1568 (2010).
[71]M. Albertí, A. Aguilar, F. Huarte-Larrañaga, J. M. Lucas, and F. Pirani, "Benzene-hydrogen bond (C_6H_6-HX) interactions: The influence of the X nature on their strength and anisotropy," J. Phys. Chem. A **118**(9), 1651–1662 (2014).
[72]M. O. Sinnokrot and C. D. Sherrill, "Highly accurate coupled cluster potential energy curves for the benzene dimer: Sandwich, T-shaped, and parallel-displaced configurations," J. Phys. Chem. A **108**(46), 10200–10207 (2004).
[73]C. D. Sherrill, T. Takatani, and E. G. Hohenstein, "An assessment of theoretical methods for nonbonded interactions: Comparison to complete basis set limit coupled-cluster potential energy curves for the benzene dimer, the methane dimer, benzene-methane, and benzene-H_2S," J. Phys. Chem. A **113**(38), 10146–10159 (2009).
[74]A. S. Mahadevi and G. N. Sastry, "Cooperativity in noncovalent interactions," Chem. Rev. **116**(5), 2775–2825 (2016).
[75]A. S. Reddy, D. Vijay, G. M. Sastry, and G. N. Sastry, "From subtle to substantial: Role of metal ions on π–π interactions," J. Phys. Chem. B **110**(6), 2479–2481 (2006).
[76]M. Rimmen, J. Matthiesen, N. Bovet, T. Hassenkam, C. S. Pedersen, and S. L. S. Stipp, "Interactions of Na^+, K^+, Mg^{2+}, and Ca^{2+} with benzene self-assembled monolayers," Langmuir **30**(30), 9115–9122 (2014).
[77]M. Duan, B. Song, G. Shi, H. Li, G. Ji, J. Hu, X. Chen, and H. Fang, "Cation ⊗ 3π: Cooperative interaction of a cation and three benzenes with an anomalous order in binding energy," J. Am. Chem. Soc. **134**(29), 12104–12109 (2012).
[78]P. Lo Nostro and B. W. Ninham, "Hofmeister phenomena: An update on ion specificity in biology," Chem. Rev. **112**(4), 2286–2322 (2012).
[79]F. Hofmeister, "Zur Lehre von der Wirkung der Salze," Arch. Exp. Pathol. Pharmakol. **24**, 247–260 (1888).
[80]R. J. Hill, D. M. Jarvie, J. Zumberge, M. Henry, and R. M. Pollastro, "Oil and gas geochemistry and petroleum systems of the Fort Worth Basin," AAPG Bull. **91**(4), 445–473 (2007).
[81]A. M. Martini, L. M. Walter, and J. C. McIntosh, "Identification of microbial and thermogenic gas components from Upper Devonian black shale cores, Illinois and Michigan basins," AAPG Bull. **92**(3), 327–339 (2008).